



Micro- and Nano-structured 3D Printed Titanium Implants with Hydroxyapatite Coating for Improved Osseointegration

Journal:	<i>Journal of Materials Chemistry B</i>
Manuscript ID	TB-ART-12-2017-003251.R1
Article Type:	Paper
Date Submitted by the Author:	31-Mar-2018
Complete List of Authors:	Jie, Qin; Jilin Province Key Laboratory of Tooth Development and Bone Remodeling, Department of Dental Implantology, School and Hospital of Stomatology, Jilin University , Yang, Dongqing; the University of Adelaide Maher, Shaheer; University of Adelaide lima-marques, Luis; The University of Adelaide, d. The Institute for Photonics and Advanced Sensing Zhou, Yanmin ; Jilin University, b. Departments of Dental Implantology, School and Hospital of Stomatology Chen, Yujie ; the university of Adelaide, School of Mechanical Engineering Atkins, Gerald; University of Adelaide, Orthopaedics and Trauma Losic, Dusan; The University of Adelaide, School of Chemical Engineering



Micro- and Nano-structured 3D Printed Titanium Implants with Hydroxyapatite Coating for Improved Osseointegration

Jie Qin,^{ab} Dongqing Yang,^{†c} Shaheer Maher,^{†a} Luis Lima-Marques,^d Yanmin Zhou,^b Yujie Chen,^e Gerald J. Atkins,^{*c} and Dusan Losic^{*a}

Received 00th January 20xx,
Accepted 00th January 20xx

DOI: 10.1039/x0xx00000x

www.rsc.org/

With the increasing demand for low-cost and more efficient dental implants, there is an urgent need for developing new manufacturing approaches and implants with better osseointegration performances. 3D printing technology can provide enormous opportunities for rapid fabrication of a new generation of patient-tailored dental implants with significantly reduced costs. This study presents the demonstration of a unique model of titanium implants based on 3D printing technology with improved osseointegration properties. The titanium alloy (Ti6Al4V) implants with micro-structured surface are fabricated with a selective laser-melting process followed by further nano-structuring with electrochemical anodization to form titania nanotubes (TNT) and subsequent bioactivation by hydroxyapatite (HA) coating. The osseointegration properties of the fabricated implants were examined using human primary osteoblasts. The results showed significantly increased protein adsorption, cell adhesion and cell spreading. The expression of the late osteoblast/osteocyte genes *GJA1* and *PHEX* was also enhanced, indicating a cell maturation effect and promotion of mineralization on the surfaces. These results suggest that 3D printing technology combined with electrochemical nano-structuring and HA modification is a promising approach for fabrication of Ti implants with improved osseointegration and provides potential alternatives to conventional dental implants.

1. Introduction

The number of dental implant procedures is steadily increasing worldwide, reaching about one million operations every year.¹ This rising demand poses a great challenge to the conventional dental implant industry. Manufacturing by casting or machining, the conventional implant production approach, is complicated, expensive, and time consuming.² Furthermore, current implants are only available in a fixed set of dimensions and therefore may not be suitable for every patient. In addition, the requirement of storing a large variety of pre-made implants could result in serious wasting of resources due to expiration and therefore making implants more expensive.² Thus, a more efficient approach for implant production and custom made on demand is highly desirable.

Three-dimensional (3D) printing is currently attracting increasing attention across many sectors opening new

horizons for fabrication of various biomedical implants and tissue engineering.³ This technology directly utilizes computer-aided design models to fabricate any desired structures, saving significant time and cost.⁴ The application of 3D printing to fabricate patient tailored implants with desirable properties will result in revolutionary improvements, among which is the flexibility in implant design to obtain different shapes of implants with tuned dimensions.⁵ More importantly, 3D printing will allow production on demand and personalized implants using computed tomography (CT) scans to create a precisely defined shape to replace a missing tooth which can be designed especially for each patient that can be fabricated very quickly in clinical environment.⁴ At the same time, the implant manufacturing companies using this technology will be able to deliver implants on request instead of massive production and storage of implants. Accordingly, 3D printing technology is emerging as a promising tool for producing new generation of medical implants. However, before putting such 3D printed dental implants into real application, it is important to investigate and optimize their performance in terms of osseointegration, a critical prerequisite for the stability and long-term survival rate of dental implants.⁶

Since the implant surface comes directly in contact with bone after insertion, many efforts have been made to modify the surface properties to improve their biointegration.^{7, 8} Early work by Buser et al.⁹ showed that a micro-roughened surface prepared by sandblasting and acid etching significantly

^a School of Chemical Engineering, The University of Adelaide, 5005, Australia.

^b Departments of Dental Implantology, School and Hospital of Stomatology, Jilin University, 130021, China.

^c Centre for Orthopaedic and Trauma Research, Adelaide Medical School, Discipline of Orthopaedics and Trauma, The University of Adelaide, 5005, Australia.

^d The Institute for Photonics and Advanced Sensing, The University of Adelaide, SA 5005, Australia.

^e School of Mechanical Engineering, The University of Adelaide, 5005, Australia.

[†] These authors equally contributed to the work. *Email - dusan.losic@adelaide.edu.au

increased osseointegration compared to smooth surfaces. Such rough topographies are believed to provide mechanical interlocking with cells. Considering that the major components of bone are nano-scale materials, it is proposed that implants with nano-surface topography could provide superior osseointegration features.¹⁰

Titania nanotubes (TNT) structures prepared by electrochemical anodization of titanium are recognized as a remarkable representative of these nanostructures.¹¹ These arrays of tiny tubes which are open at the top and closed at bottom can be prepared with well control over dimensions (diameters 10-300 nm and lengths 0.5 to 300 μm) and they are well explored for drug-delivery applications.¹² Electrochemical anodization is a scalable, cost-effective and simple fabrication process that can be implemented for modifications of medical implants using most clinically proved metals at industrial scale.¹³ Several studies have demonstrated that TNT structures could promote osteoblast cell adhesion, proliferation and enhance the ingrowth of bone and vascular tissues.¹⁴⁻¹⁷ Additionally, the residual fluoride in TNT resulting from the anodization process could also favor the implant osseointegration.¹ The first concept to demonstrate engineering of new 3D printed Ti implants (3D-Ti) for drug delivery applications is recently demonstrated by our group showing promising applications for delivery of anti-cancer drugs and localized cancer therapy.¹⁸

In this work we propose an approach to further improve the osseointegration performance of 3D printed Ti alloy implants by combining 3D printing technology, surface nanoengineering and chemical modification. The concept is based on the idea to develop advanced 3D printed implants with dual micro- and nano-topography (3D-Ti-TNT) fabricated by 3D printing and electrochemical anodization, followed by hydroxyapatite (HA) surface functionalization as depicted in Fig. 1. The enhancement of osseointegration performance of 3D implants using HA is proposed due to its chemical similarities to bone mineral.¹⁹⁻²¹ HA is clinically approved for surface coating of medical implants to promote bone healing and apposition, leading to faster fixation and better clinical outcomes.¹⁹⁻²¹ Successful synthesis of HA on titania nanotubes has been achieved by a simple and efficient alternative immersion method (AIM), consisting of successive immersion of the implants into $\text{Ca}(\text{OH})_2$ and $(\text{NH}_4)_2\text{HPO}_4$ for repeated cycles.²² The implants after each fabrication step were characterized by different techniques to show surface morphology and

chemical composition. The osseointegration properties of fabricated implants were evaluated by protein adsorption, cell adhesion, morphology and gene expression. The results obtained suggest that the fabricated implants could be a promising alternative for the fabrication of patient-specific dental implants.

2. Experimental

2.1. 3D printing of Ti implants

Titanium alloy powder (Ti6Al4V) was used for printing the implants in the forms of square strips ($1.2 \times 1.2 \text{ cm}^2$) with a selective laser melting machine (3D System ProX 200 (Phenix Systems PXM)), equipped with 300W Laser (1070 nm at 50% power), in the presence of an Argon atmosphere ($\sim 500 \text{ ppm O}_2$). A thin even layer of the metal powder was deposited across a build plate and then the selected areas of the powder were precisely melted by the high power focused laser. This process is repeated building up, layer by layer, till reaching the desired thickness ($\sim 0.6 \text{ mm}$), and generated the implants accordingly. The resulting implants are referred to as 3D-Ti throughout this study. Commercially available Titanium foil (Sigma-Aldrich, Sydney, Australia), referred to as Ti, was also cut in the same size as control.

2.2. Fabrication of 3D printed Ti implants with TNT layer

3D-Ti was cleaned by sonication in ethanol for 10 min, followed by drying in N_2 . After this, TNT layer was fabricated onto the surface by electrochemical anodization. During the process, 3D-Ti served as anode and a thin Ti foil served as cathode. Both of the electrodes were immersed in ethylene glycol electrolyte containing ammonium fluoride (0.1M), lactic acid (1.5M) and water (5 vol %). A special electrochemical setup designed in our laboratory was used, and the whole system was maintained at 60°C under constant steering on a magnetic stirrer (50 rpm). A constant voltage of 60 V was applied for 15 min. A computer-aided power supply (Agilent) was used to supply the desired voltage and was controlled using LabView program (National Instruments). After anodization, the samples were washed with MilliQ water thoroughly and dried in air. The resulting implants are referred to as 3D-Ti-TNT.

2.3. Surface functionalization of 3D-Ti-TNT with hydroxyapatite (HA) coating

HA coating on the 3D-Ti-TNT was performed by Kodama's

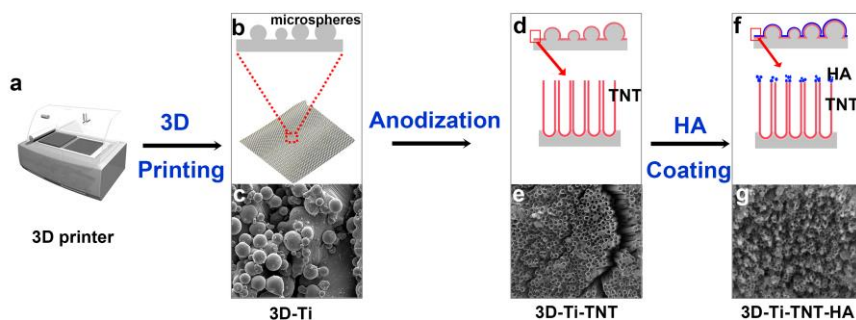


Figure 1. Scheme showing the fabrication of 3D printed Ti alloys implants with dual micro- and nano-topography fabricated by combining 3D printing, electrochemical anodization, and bioactivation by hydroxyapatite (HA) coating. (a) 3D printer. (b-c) Scheme and SEM image showing typical surface topography of 3D printed implants. (d-e) Scheme and SEM image of electrochemically engineered implants with titania nanotube layer. (f-g) Scheme and SEM image of implants after HA coating.

alternative immersion method (AIM)²². Fifteen implants were separately placed onto a custom designed holder, which permitted all TNT layers to be exposed. The holder was first manually immersed in 200 ml of saturated Ca(OH)₂ for 1 min at room temperature. Subsequently, it was manually immersed in 200 ml of (NH₄)₂HPO₄ (0.02M) for same time. This was repeated for 5 cycles. Between each soaking step and after each cycle, the implants were dipped in 200 ml of MilliQ water for 1 min without any shaking. Finally, the implants were left to dry at room temperature and referred to as 3D-Ti-TNT-HA through out this study.

2.4. Characterization of prepared implants

Surface morphology of the prepared implants was characterized by a field emission scanning electron microscope (SEM, FEI Quanta 450) working at 10kv. Prior to SEM examination, implants were coated with platinum (5 nm thickness). Energy-dispersive X-ray spectroscopy (EDS) was also recorded to analyse the elemental composition of the implants. X-Ray Diffraction (XRD) patterns were also employed using Rigaku Miniflex diffractometer operating at 40 kV and 15mA. The scan range was from 30° to 80° (2θ) at a step size of 0.02°. The mechanical properties of the implants were assessed by a nanoindentation system (IBIS, M/S Fisher-Cripps Laboratory, Australia). Load-controlled indentation with a maximum load of 200 mN was performed on the polished surface of the implants, with a loading rate of 2.5 mN/s, which represented the static response of the material.²³ The Oliver-Pharr method 2 was used to quantify the elastic modulus (*E*) and hardness (*H*).

2.5. Protein adsorption

All implants were cut to a standard size (6 x 6 mm²) and sterilized by UV irradiation for 1h on both sides. Protein solution, also used as culture media, was prepared with α-modified minimal essential medium (α-MEM, Gibco, NY, USA) supplemented with foetal bovine serum (10 vol %), HEPES (10 mM), L-Glutamine (0.2 M) and penicillin/streptomycin (1 vol %). Each Ti, 3D-Ti, 3D-Ti-TNT, and 3D-Ti-TNT-HA implant (in triplicate) was placed in a single well of the 48-well plate. 250 μl of the protein solution was added onto each implant surface and incubated at 37 °C for 1.5 h. Unattached proteins were washed away with PBS. Attached proteins were fixed with neutral formalin (10%) and stained with crystal violet (1%) for 20 min. The excess stain was removed by washing in water. The protein-associated stain was then extracted with acetic acid (10 vol %, 200 μl well⁻¹) for 20 min and the absorbance at 570 nm was measured by spectrophotometry.

2.6. Cell Adhesion

Human osteoblast-like cells grown from bone samples were obtained with patient informed consent, as previously described.²⁴ Cells were cultured in α-modified minimal essential medium (α-MEM, Gibco, NY, USA) supplemented with foetal bovine serum (10 vol %), HEPES (10 mM), L-Glutamine (0.2 M) and penicillin/streptomycin (1 vol %) (all from Life Technologies). After reaching confluence, osteoblast cells were removed from culture flasks using collagenase-2, trypsin, and suspended at a density of 2 × 10⁵ cells ml⁻¹. A 250

μl aliquot (containing 5 × 10⁴ cells) was added onto each implant (Ti, 3D-Ti, 3D-Ti-TNT, and 3D-Ti-TNT-HA (in triplicate)). After incubating for 2h, unattached cells were removed by PBS washing. Attached cells were fixed with neutral formalin (10%) and stained with 4',6-Diamidino-2-Phenylindole (DAPI) (1μg ml⁻¹). Cell numbers in three random fields from each sample were counted under a fluorescence microscope (Olympus_BX51).

2.7. Cell Morphology study by confocal microscopy

Cells were seeded on to each implant (Ti, 3D-Ti, 3D-Ti-TNT, and 3D-Ti-TNT-HA) in a 48-well plate. 24h after seeding, the media were removed. Implants with cells on the surfaces were gently washed by PBS and fixed with neutral buffered formalin (10%). Attached cells were stained with phalloidin-TRITC (10 μM) (Sigma) and DAPI (1μg ml⁻¹) in PBS for 1h. Cell morphology was observed under a confocal laser-scanning microscope (Olympus FV3000). Phalloidin-TRITC was excited at 561nm and DAPI at 405nm.

2.8. Cell Morphology study by SEM

Cells were seeded on to each implant (Ti, 3D-Ti, 3D-Ti-TNT, and 3D-Ti-TNT-HA) at a density of 5 × 10⁴ in a 48-well plate. 3 days after seeding, the media were removed and changed into differentiation medium (α-MEM with foetal bovine serum (10%), ascorbate-2-phosphate (50 μg ml⁻¹) and potassium dihydrogen phosphate (1.8 mM)). 7 days later, implants with cells on the surfaces were gently washed by PBS and fixed in glutaraldehyde (1.25%) (Sigma-Aldrich, Sydney, Australia) for 24h. A post-fix in osmium tetroxide (2%) for 30 min was also performed. After that, cells were dehydrated serially in 70%, 90%, 100% ethanol, 100% hexamethyldisilazane (HMDS): 100% ethanol (1:1) solution, and 100% HMDS. After drying, implants were mounted on SEM holders, coated with 5nm thick layer of platinum, and observed under a SEM.

2.9. Gene expression analysis

The expression of *GJA1* and *PHEX* was analysed by using reverse transcription-quantitative polymerase chain reaction (RT-qPCR). SaOS2 human osteoblast-like cells, a well-established cell line for gene analysis, were seeded on to each implant at a density of 1 × 10⁶. After reaching confluence, the media were changed into differentiation medium as described above. The media were replaced at 3 or 4 -day intervals. After 7 days of differentiation, RNA was harvested from each sample using Trizol reagent (Life Technologies, NY, USA) and was reverse transcribed into cDNA using the iScript RT kit (BioRad, CA, USA) as described elsewhere.²⁵ SYBR Green Fluor qPCR Mastermix (Qiagen, Limburg, The Netherlands) was used to perform RT-qPCR in a CFX Connect thermocycler (BioRad) with primer sequences published previously.²⁶ Primers were synthesized by Geneworks (Thebarton, SA, Australia). Relative gene expression was calculated using 2^{-ΔΔCt} method and normalized to the expression of 18s.

2.10. Statistical analysis

Data are expressed as the means ± SEM and were analysed using one-way analysis of variance (ANOVA) with Tukey's multiple comparison test. A p-value <0.05 was considered to indicate a statistically significant difference.

3. Results and Discussion

3.1 Characterization of Nanostructured and HA Functionalized 3D Printed Implants

Scanning electron microscope (SEM) images of the surface morphology of prepared implants are presented in Fig. 2. As shown in Fig. 2a, 3D printed Ti implants (3D-Ti) were covered by numerous microspheres of sizes ranging from 5-20 μm (average $\sim 12\mu\text{m}$) in diameter. Higher resolution images showed that these structures were fused to the underlying surface, and were highly interconnected (Fig. 2b), suggestive of a stable, micro-rough surface. These microspheres result from partial melting of the alloy powder used during the selective laser melting process. This topography contrasted sharply with that of commercially available Ti (Ti), which possessed a relatively smooth surface as seen in Fig. 2c.

As a result of electrochemical anodization, a well-ordered titania nanotube (TNT) layer was generated on the entire surface of the 3D printed Ti implant, including the microspheres (Fig. 2d and 2e) and the underlying surface (Fig. 2e and f). A powder sintering route using the space-hold technique has also been reported to produce porous Ti

implants.²⁷ However, the pore-size in such implants is distributed within a wide range. Therefore, the reproducibility of the porous structures to control the physicochemical properties of the implant is challenging. By comparison, the implant in this study was fabricated with reproducibly uniform nanotubes with an average individual tube diameter of ~ 120 nm, length of $\sim 3\mu\text{m}$ and density of $\sim 5 \times 10^9$ nanotubes/ cm^2 . As expected, cracks were evident on the TNT layers due to the radial outgrowth of nanotubes on the curved surfaces. However, these cracks do not compromise the stability of the TNT layer and potentially allow for additional amounts of therapeutics to be loaded.^{18, 28-30} These findings confirm the successful fabrication of an advanced implant with combined dual micro- and nano-topography, represented by the microspheres and TNT, respectively.

SEM images of prepared 3D-Ti-TNT implants after HA immersion treatment are presented in Fig. 2g and 2h. Crystalline deposits were found homogeneously distributed on the implant surface (Fig. 2g). TNT structures were still visible as shown in the higher resolution image (Fig. 2h). These results are in accordance with Kodama's work, in which HA coating was successfully fabricated on TNT by HA immersion

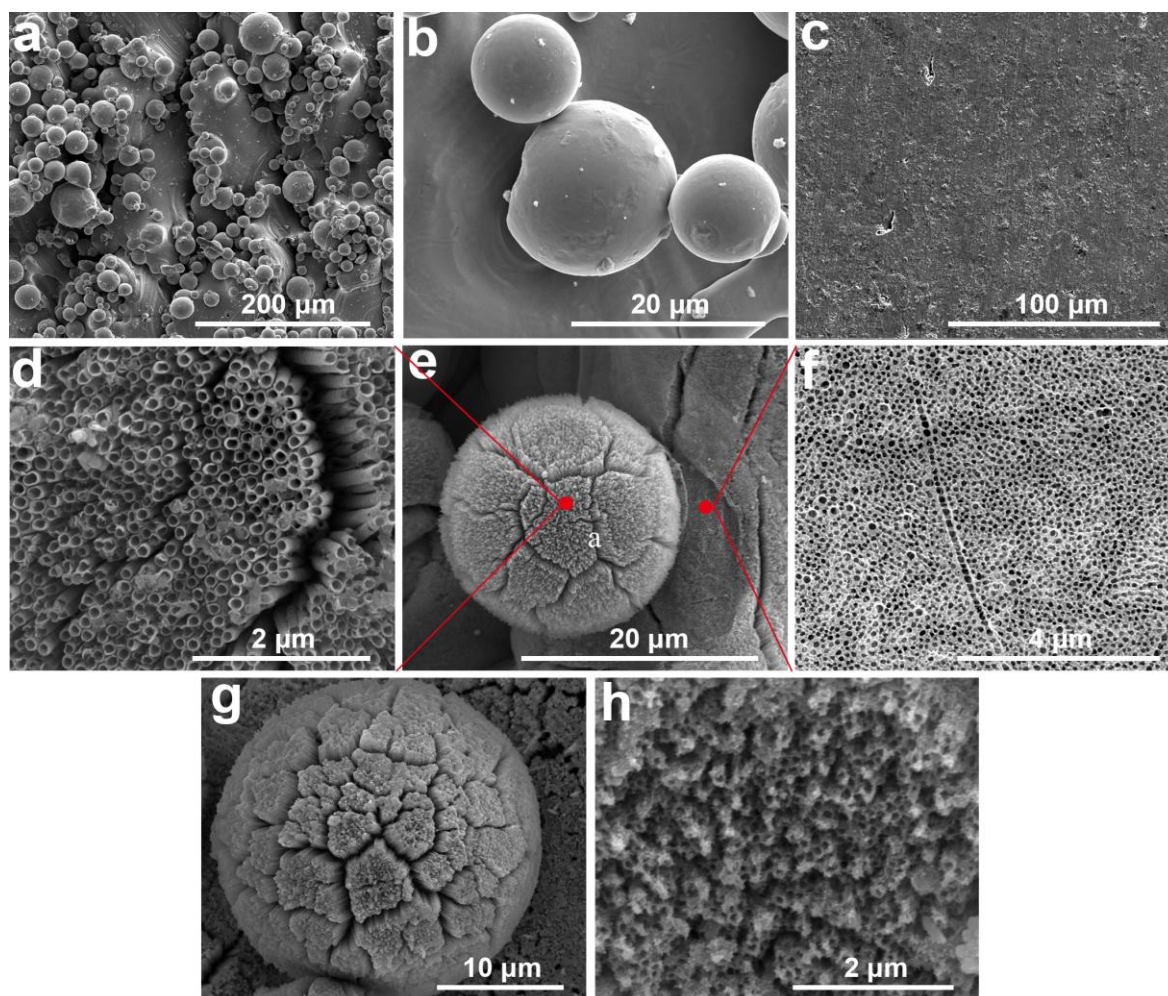


Figure 2. SEM images of 3D-Ti (a-b), Ti (c), 3D-Ti-TNT (d-f) and 3D-Ti-TNT-HA (g-h). (a) 3D-Ti was covered by microspheres of various sizes. (b) High resolution image showing microspheres were fused to the underlying surface, and were highly interconnected. (c) Pure Ti foil possessed a relatively smooth surface (i.e. no micro-features). (d-f) TNT were formed on the entire surface of 3D Ti, including the microspheres (d,e) and the underlying surfaces (e,f). (g) Crystalline deposits were found on the implant surface and (h) the nanotubes were still visible after HA coating.

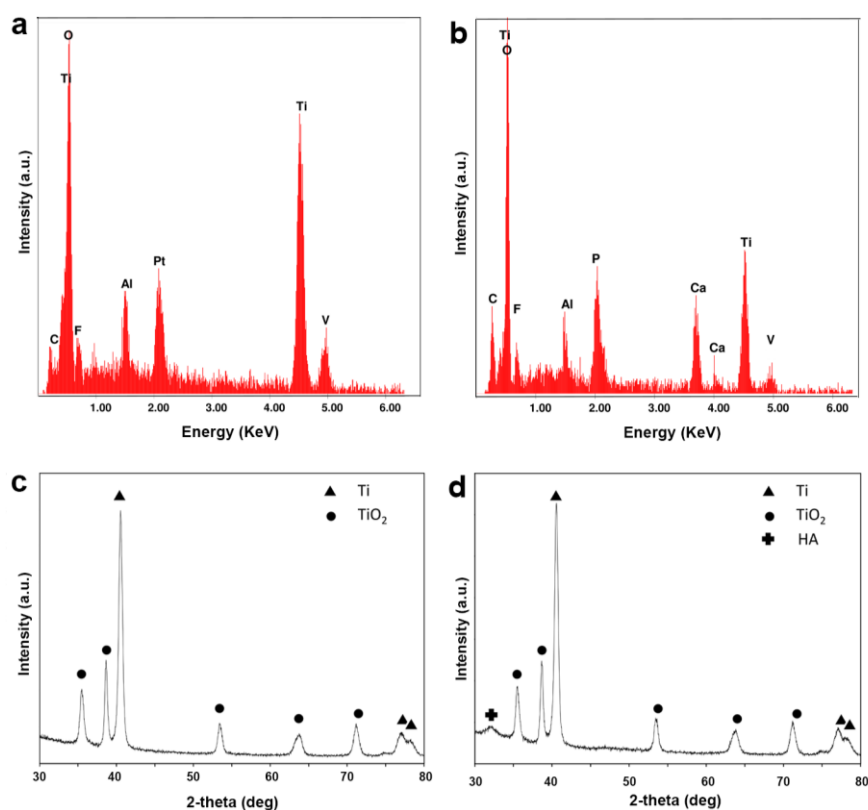


Figure 3. (a-b) EDS and (c-d) XRD spectrum. EDS spectrum of 3D-Ti-TNT before (a) and after (b) HA treatment. Significant Ca and P peaks appeared after HA treatment (b). XRD spectrum of 3D Ti TNT before (c) and after (d) HA treatment. HA peaks appeared after HA treatment (d).

treatment.²¹ Gu et al.³¹ proposed the mechanism of HA formation to result from the reaction of the titanium oxide layer with hydroxide to form hydrogen metatitanate: $\text{TiO}_2 + \text{OH}^- \rightarrow \text{HTiO}_3^-$. The resulting negatively charged surface promoted adsorption of Ca^{2+} and formation of calcium titanate. This titanate then adsorbed HPO_4^{2-} in the solution of $(\text{NH}_4)_2\text{HPO}_4$ to form calcium phosphate nuclei. Subsequent HA formation and crystallization would then readily occur.

To evaluate the chemical nature of the crystalline deposits on the implant surface, energy dispersive X-ray spectroscopy (EDS) was performed before (Fig. 3a) and after (Fig. 3b) the HA treatment. Fig. 3b shows significant peaks of Ca and P after HA treatment, indicating a successful formation of Ca-P deposit, with a Ca:P ratio of 1.53, which approximates the theoretical Ca:P ratio (1.67) of HA, confirming the formation of HA layer on the implant surface.³² It is noteworthy that fluoride peaks appeared on the implant surface with TNT. These fluoride ions were deriving from the anodization electrolyte and incorporated into the TNTs structures. It is worth mentioning that the presence of F^- ions are claimed to be favorable to the osseointegration of implants.³³

X-ray diffraction (XRD) graphs were also recorded before (Fig. 3c) and after (Fig. 3d) the HA treatment. According to the reference data JCPDS-0432, HA peaks were present after the HA treatment (Fig. 3d). This additionally confirmed the formation of HA on the implant surface.

The elastic modulus (E) of the implant was measured to be 109.9 ± 1.8 GPa, which was consistent with the reported values of the biomedical Ti6Al4V alloy (110-114 GPa).³⁴ The hardness (H) of the implant reached 4.84 ± 0.12 GPa, compared to 3.28 - 3.39 GPa in the wrought Ti6Al4V.^{34, 35} According to the relationship between yield strength (σ_y) and hardness: $H = 3\sigma_y$,⁵ yield strength of the implant was estimated to be ~ 1.6 GPa, which clearly surpassed the American Society for Testing and Materials (ASTM) standard (795 MPa).³⁶ Compared with the porous implant produced by space-hold technique, which has a yield strength of 60 MPa,²⁷ the 3D printed implant in this study could provide much higher yield strength. It is presumably strong enough to resist handling during implantation and in vivo loading. Notably, wear resistance is closely related to the ratio between H and E , the so-called plasticity index.³⁷ Materials with a higher plasticity index exhibit greater wear resistance. Therefore, one could expect that, compared to wrought Ti6Al4V, our 3D printed Ti6Al4V with similar elastic modulus, but higher hardness would exhibit increased wear resistance.³⁸

3.2. Protein adsorption

When a material is implanted, proteins in the surrounding tissues and plasma would be expected to spontaneously adsorb onto the implant surface. This protein layer could mediate the subsequent cell performance, playing an important role during the osseointegration process.³⁹ The

protein adsorption properties were therefore tested and found to be: 3D-Ti-TNT-HA > 3D-Ti-TNT > 3D-Ti > Ti (Fig. 4a). The increase in protein adsorption on 3D-Ti and 3D-Ti-TNT could be attributed to the increased surface roughness due to the microspheres and nanostructures.⁴⁰

Another noteworthy finding in these experiments was that 3D-Ti-TNT-HA had a significant increase in protein adsorption compared with others samples. The total protein adsorbed on 3D-Ti-TNT-HA was 92-folds that of Ti, 60-folds that of 3D-Ti, and 5-folds that of 3D-Ti-TNT. This is in accordance with a recent study, in which serum proteins preferably adsorbed onto an HA coated surface but not onto Ti.⁴¹ Wang et al. pointed out that the possible reason might be electrostatic force.⁴² Ionic Ca^{2+} and PO_4^{3-} groups on HA surfaces could serve as the protein binding sites, with calcium sites binding negatively charged groups, such as carboxylate group and carbonyl group, and phosphate sites binding positively charged groups, including amino, aromatic and guanido groups, on the protein molecules.⁴²

3.3. Cell adhesion

Cell adhesion is the most critical event that occurs when bone cells come into contact with an implant surface, which is crucially important for the subsequent cellular behaviour.⁴³ Additionally, early adhesion of bone cells could competitively inhibit bacterial adhesion.⁴⁴ Therefore, cell adhesion on Ti, 3D-Ti, 3D-Ti-TNT, and 3D-Ti-TNT-HA was evaluated after 2h of incubation. As shown in Fig. 4b, 3D-Ti-TNT-HA exhibited significantly increased cell adhesion. This is in accordance with the above protein adsorption results. Previous studies reported a similar correlation, proposing that this occurred due to adhered proteins being extracellular matrix proteins, such as fibronectin and vitronectin, which efficiently promote cell attachment.^{41, 45}

3.4. Cell Morphology

The response of osteoblastic cells to these surfaces was tested using human primary bone-derived cells, previously termed 'NHBC'. These represent a spectrum of early osteoblast-osteocyte differentiation stages and provide a clinically relevant model for the current application since they

are derived from patients receiving an orthopaedic implant.^{46, 47} The morphology of osteoblasts on the different implant surfaces at an early stage (24h) was examined by confocal microscopy (Fig. 5). Cytoskeleton was stained with phalloidin-TRITC (red) and nucleus was stained with DAPI (blue). Results indicated that cells on Ti spread widely, whereas cells on the other (3D) surfaces appeared to retain a smaller footprint, with an increased number of dendritic-like connections between adjacent cells. In the bone, such intercellular connectivity allows for the transfer of biochemical signals between cells, and in mature bone interconnected osteocytes in this way form a functional syncytial network.^{48, 49} Moreover, cells on 3D-Ti, 3D-Ti-TNT and 3D-Ti-TNT-HA had a larger nuclear:cytoplasm ratio compared with those on Ti, consistent with a more differentiated cell phenotype.⁵⁰ Confocal microscopy was not able to distinguish the cell morphologies when the cell number increased with time, due to the general high degree of confluency of the cultures. SEM was therefore employed to examine cell morphology after 7 days culture (Fig. 6). Cells on Ti spread in a 2D manner and remained flat and spindle shaped (Fig. 6a), whereas those on 3D-Ti exhibited a plump, polygonal morphology (Fig. 6b). Cells on 3D-Ti-TNT began to exhibit a stellate shape with long, slender dendritic processes, suggesting a further differentiated morphology (Fig. 6c).⁵¹ Cells cultured on 3D-Ti-TNT-HA exhibited a more prominent stellate shape, with many cell processes and pseudopodia (Fig. 6 d and 6e). Similar observations were reported by Kim et al., who found that the direction of cell spreading was more diverse on Ti if a HA coating was applied.⁵² Overall, our findings suggest that cells cultured on 3D-Ti-TNT-HA had a more mature and differentiated, osteocyte-like morphology.⁵³ This finding is consistent with the study of Gu et al.,³¹ indicating superior differentiated morphology of osteoblasts on a HA-deposited TNT surface. The advantage of our material lies in that, instead of fabricating TNT onto a flat Ti surface, as performed by Gu et al., we fabricated TNT onto 3D-Ti. This 3D-Ti has an osseoinductive micro-rough surface and can be tailored to any desired dimension.

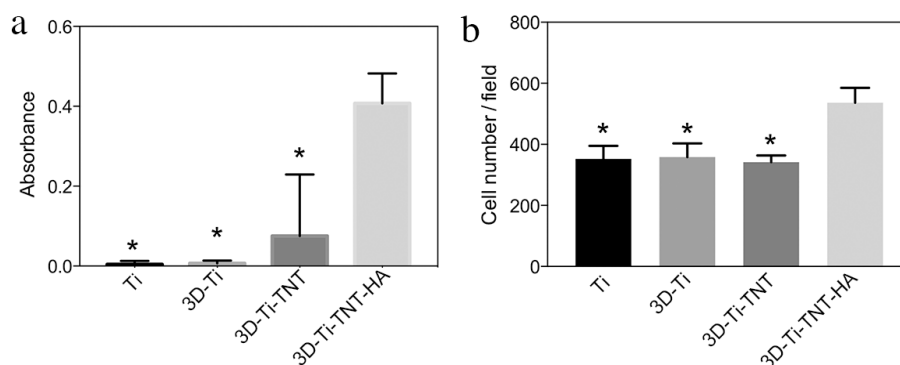


Figure 4. (a) Protein adsorption and (b) cell adhesion on Ti, 3D-Ti, 3D-Ti-TNT, and 3D-Ti-TNT-HA. (a) 3D-Ti-TNT-HA had a significant increase in protein adsorption. (b) 3D-Ti-TNT-HA significantly increased cell adhesion. Data shown are means \pm SEM. Significant difference to 3D-Ti-TNT-HA is indicated by * ($p < 0.05$).

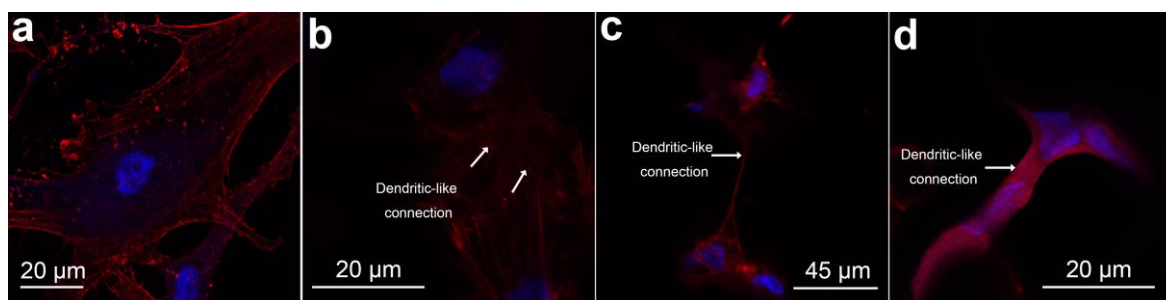


Figure 5. Confocal microscopy images of human primary osteoblasts on (a) Ti, (b) 3D-Ti, (c) 3D-Ti-TNT, and (d) 3D-Ti-TNT-HA after 24h of culture. (a) Cells on Ti spread widely. (b-d) Cells on 3D surfaces had a larger nuclear:cytoplasm ratio and retained a smaller footprint, with an increased number of dendritic-like connections between adjacent cells, indicative of a more differentiated cell phenotype.

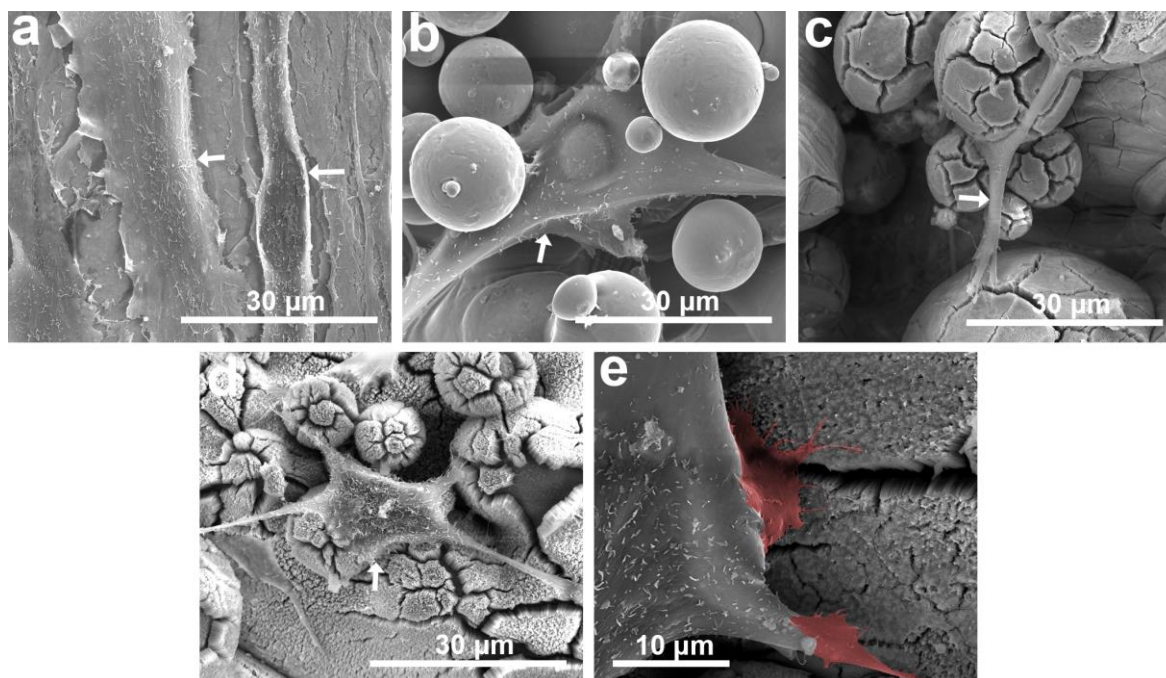


Figure 6. SEM images of human primary osteoblasts on (a) Ti, (b) 3D-Ti, (c) 3D-Ti-TNT, and (d,e) 3D-Ti-TNT-HA after 7 days of culture. (a) Cells on Ti spread flatly and remained a spindle-like shape. (b) Cells on 3D-Ti showed a plump, polygonal shape. (c) Cells on 3D-Ti-TNT exhibited a stellate shape with long dendritic processes. (d) Cells on 3D-Ti-TNT-HA exhibited a more prominent stellate shape, with many cell processes and pseudopodia (e) suggesting a further differentiated morphology. White arrows indicate cells. Red colours indicate pseudopodia.

3.5. Gene expression

The expression of *GJA1*, encoding connexin 43 (Cx43), the principal protein component of functional gap-junctions in bone cell networking and a marker of mature osteocytes,²⁶ was increased in cultures on 3D-Ti, 3D-Ti-TNT, and 3D-Ti-TNT-HA, suggesting a maturation effect of the 3D structure (Fig. 7a). The expression of the gene *PHEX*, encoding phosphate-regulating gene with homologies to endopeptidases on the X chromosome, an osteocyte maker that promotes mineralization,⁵⁴ was also significantly increased on 3D-Ti-TNT-HA compared with the other three surfaces (Fig. 7b), indicating that this surface could better promote osteoblast/osteocyte-mediated mineralization and differentiation. Both calcium and phosphate ions, which could be released from the HA substrate, are known promoters of biomineralisation and osteoblast/osteocyte differentiation.^{55, 56}

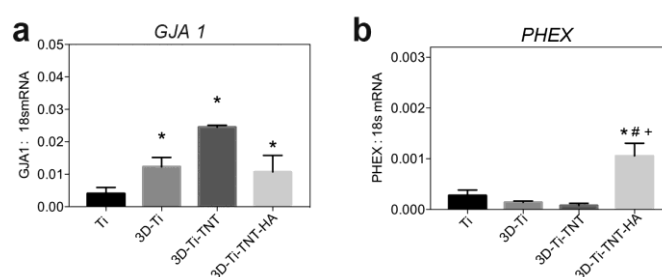


Figure 7. Gene expression of *GJA1* and *PHEX* in SAOS2 cells plated on different implant surfaces after 7 days of culture. (a) The expression of *GJA1* was increased on 3D structure. (b) The expression of *PHEX* was significantly increased on 3D-Ti-TNT-HA. Data shown are means of three experimental replicates \pm SEM. Significant differences to expression on Ti are indicated by * ($p < 0.05$). Significant differences to expression on 3D-Ti are indicated by # ($p < 0.05$). Significant differences to expression on 3D-Ti-TNT are indicated by + ($p < 0.05$).

4. Conclusions

This current study presents advanced 3D printed and nanostructured Ti alloy implants modified with HA, to provide improved osseointegration properties based on enhanced protein adsorption, cell adhesion, cell spreading and mature osteoblast gene expression patterns. These implants were fabricated using a combination of 3D printing technology, electrochemical surface nanoengineering and chemical coating using HA. 3D printed Ti implants have characteristic micro-scale roughness, due to the presence of microspherical structures from laser sintering process combine with array of nanotubular structures additionally introduced by electrochemical anodization while retaining the micro-particle arrangement. These implants were further functionalized by HA coating via an alternative immersion method in order to further improve their bone integration performances. The resulting implants significantly promoted protein adsorption, osteoblast cell adhesion, spreading, and increased the expression of certain genes related to osteoblast differentiation and mineralisation. These results are explained by combined and synergetic impact of dual topography and HA chemistry. The results suggest that nanostructured and functionalised 3D-Ti-TNT-HA has promise in the manufacture of improved dental implants to current conventional implants. In addition, 3D-Ti-TNT-HA implant could be developed as a drug releasing system with extra therapeutic functions, achieved by loading drugs (e.g. anti-inflammatory drugs, and antibiotics) into the titania nanotubes. Further bone response studies using animal model are required before the clinical application of this implant.

Conflicts of interest

There are no conflicts of interest to declare.

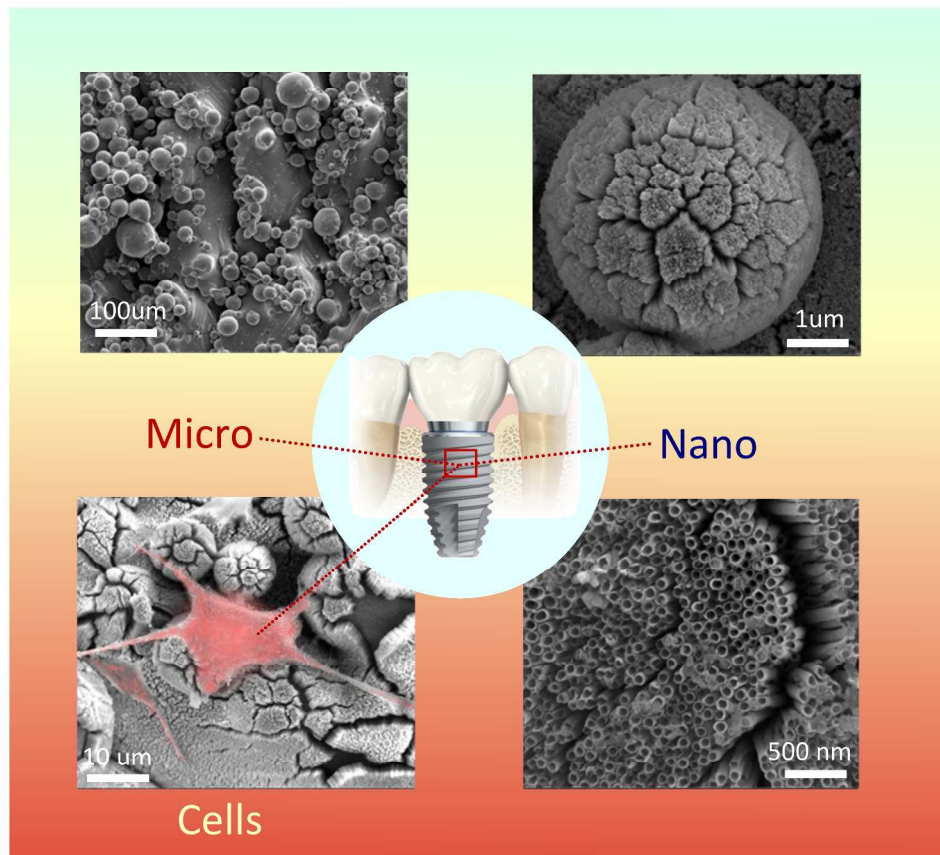
Acknowledgements

Authors acknowledge the financial support provided to S.M. by the Australian Government Training Program Scholarship, ARC grant funded supplementary scholarship and Forrest George and Sandra Lynne Young Supplementary Scholarship. This work was performed in part at the OptoFab node of the Australian National Fabrication Facility utilizing Commonwealth and SA State Government funding. Authors thank Dr. Animesh Basak, Dr. Agatha Labrinidis, Ms Ruth Williams, and Mr. Ken Neubauer from Adelaide Microscopy (AM) center for providing technical support for confocal microscopy and SEM. Also acknowledged is the support from Pro. Zonghan Xie at School of Mechanical Engineering, The University of Adelaide, and Dr. Asiri R. Wijenayaka at the Centre for Orthopaedic and Trauma Research, The University of Adelaide.

References

- 1 L. Le Guehennec, A. Soueidan, P. Layrolle and Y. Amouriq, *Dent Mater*, 2007, **23**, 844-854.
- 2 V. Bhasin, M. R. Bodla and Massachusetts Institute of Technology. Engineering Systems Division., *Impact of 3D printing on global supply chains by 2020*, 2014.
- 3 U. Kalsoom, P. N. Nesterenko and B. Paull, *Rsc Adv*, 2016, **6**, 60355-60371.
- 4 D. Radenkovic, A. Solouk and A. Seifalian, *Med Hypotheses*, 2016, **87**, 30-33.
- 5 C. L. Ventola, *P T*, 2014, **39**, 704-711.
- 6 R. Adell, U. Lekholm, B. Rockler and P. I. Branemark, *Int J Oral Surg*, 1981, **10**, 387-416.
- 7 N. Jiang, S. S. Zhu, J. H. Li, L. Zhang, Y. M. Liao and J. Hu, *Rsc Adv*, 2016, **6**, 49954-49965.
- 8 M. M. Lu, D. Shao, P. Wang, D. Y. Chen, Y. D. Zhang, M. Q. Li, J. H. Zhao and Y. M. Zhou, *Rsc Adv*, 2016, **6**, 82688-82697.
- 9 D. Buser, R. K. Schenk, S. Steinemann, J. P. Fiorellini, C. H. Fox and H. Stich, *J Biomed Mater Res*, 1991, **25**, 889-902.
- 10 G. Mendonca, D. B. Mendonca, F. J. Aragao and L. F. Cooper, *Biomaterials*, 2008, **29**, 3822-3835.
- 11 M. Karlsson, E. Palsgard, P. R. Wilshaw and L. Di Silvio, *Biomaterials*, 2003, **24**, 3039-3046.
- 12 K. Gulati, M. S. Aw, D. Findlay and D. Losic, *Ther Deliv*, 2012, **3**, 857-873.
- 13 D. Losic and S. Simovic, *Expert Opin Drug Deliv*, 2009, **6**, 1363-1381.
- 14 K. Gulati, S. Maher, D. M. Findlay and D. Losic, *Nanomedicine (Lond)*, 2016, **11**, 1847-1864.
- 15 D. Losic, M. S. Aw, A. Santos, K. Gulati and M. Bariana, *Expert Opin Drug Deliv*, 2015, **12**, 103-127.
- 16 R. A. Gittens, T. McLachlan, R. Olivares-Navarrete, Y. Cai, S. Berner, R. Tannenbaum, Z. Schwartz, K. H. Sandhage and B. D. Boyan, *Biomaterials*, 2011, **32**, 3395-3403.
- 17 S. L. Wu, Z. Y. Weng, X. M. Liu, K. W. K. Yeung and P. K. Chu, *Adv Funct Mater*, 2014, **24**, 5464-5481.
- 18 S. Maher, G. Kaur, L. Lima-Marques, A. Evdokiou and D. Losic, *ACS Appl Mater Interfaces*, 2017, **9**, 29562-29570.
- 19 R. S. Faeda, R. Spin-Neto, E. Marcantonio, A. C. Guastaldi and E. Marcantonio, Jr., *Microscopy research and technique*, 2012, **75**, 940-948.
- 20 R. A. Surmenev, M. A. Surmeneva and A. A. Ivanova, *Acta Biomater*, 2014, **10**, 557-579.
- 21 I. H. Orenstein, D. P. Tarnow, H. F. Morris and S. Ochi, *Journal of Periodontology*, 1998, **69**, 1404-1412.
- 22 A. Kodama, S. Bauer, A. Komatsu, H. Asoh, S. Ono and P. Schmuki, *Acta Biomater*, 2009, **5**, 2322-2330.
- 23 S. O'Brien, J. Shaw, X. Zhao, P. V. Abbott, P. Munroe, J. Xu, D. Habibi and Z. Xie, *J Biomech*, 2014, **47**, 1060-1066.
- 24 G. J. Atkins, K. J. Welldon, A. R. Wijenayaka, L. F. Bonewald and D. M. Findlay, *Am J Physiol-Cell Ph*, 2009, **297**, C1358-C1367.
- 25 M. Prideaux, A. R. Wijenayaka, D. D. Kumarasinghe, R. T. Ormsby, A. Evdokiou, D. M. Findlay and G. J. Atkins, *Calcified Tissue Int*, 2014, **95**, 183-193.
- 26 D. Yang, A. G. Turner, A. R. Wijenayaka, P. H. Anderson, H. A. Morris and G. J. Atkins, *Molecular and cellular endocrinology*, 2015, **412**, 140-147.
- 27 C. Caparros, M. Ortiz-Hernandez, M. Molmeneu, M. Punset, J. A. Calero, C. Aparicio, M. Fernandez-Fairen, R. Perez and F. J. Gil, *J Mater Sci Mater Med*, 2016, **27**, 151.
- 28 K. Gulati, M. Kogawa, M. Prideaux, D. M. Findlay, G. J. Atkins and D. Losic, *Mat Sci Eng C-Mater*, 2016, **69**, 831-840.
- 29 K. Gulati, M. S. Aw and D. Losic, *Nanoscale Res Lett*, 2011, **6**.

- 30 K. Gulati, G. J. Atkins, D. M. Findlay and D. Losic, *Proc Spie*, 2013, **8812**.
- 31 Y. X. Gu, J. Du, J. M. Zhao, M. S. Si, J. J. Mo and H. C. Lai, *J Biomed Mater Res B Appl Biomater*, 2012, **100**, 2122-2130.
- 32 G. Ciapetti, G. Di Pompo, S. Avnet, D. Martini, A. Diez-Escudero, E. B. Montufar, M. P. Ginebra and N. Baldini, *Acta Biomater*, 2017, **50**, 102-113.
- 33 L. F. Cooper, Y. Zhou, J. Takebe, J. Guo, A. Abron, A. Holmen and J. E. Ellingsen, *Biomaterials*, 2006, **27**, 926-936.
- 34 M. Niinomi, *Materials Science and Engineering: A*, 1998, **243**, 231-236.
- 35 N. Poondla, T. S. Srivatsan, A. Patnaik and M. Petraroli, *Journal of Alloys and Compounds*, 2009, **486**, 162-167.
- 36 ASTM International., *Journal*, 2002, volumes.
- 37 A. Leyland and A. Matthews, *Wear*, 2000, **246**, 1-11.
- 38 S. K. Kim, J. B. Lee, J. Y. Koak, S. J. Heo, K. R. Lee, L. R. Cho and S. S. Lee, *Journal of oral rehabilitation*, 2005, **32**, 346-350.
- 39 E. N. Mpoyi, M. Cantini, P. M. Reynolds, N. Gadegaard, M. J. Dalby and M. Salmeron-Sanchez, *Acs Nano*, 2016, **10**, 6638-6647.
- 40 D. D. Deligianni, N. Katsala, S. Ladas, D. Sotiropoulou, J. Amedee and Y. F. Missirlis, *Biomaterials*, 2001, **22**, 1241-1251.
- 41 K. L. Kilpadi, P. L. Chang and S. L. Bellis, *J Biomed Mater Res*, 2001, **57**, 258-267.
- 42 K. Wang, C. Zhou, Y. Hong and X. Zhang, *Interface Focus*, 2012, **2**, 259-277.
- 43 B. Joddar and Y. Ito, *J Mater Chem*, 2011, **21**, 13737-13755.
- 44 A. G. Gristina, *Science*, 1987, **237**, 1588-1595.
- 45 D. M. Rivera-Chacon, M. Alvarado-Velez, C. Y. Acevedo-Morantes, S. P. Singh, E. Gultepe, D. Nagesha, S. Sridhar and J. E. Ramirez-Vick, *J Biomed Nanotechnol*, 2013, **9**, 1092-1097.
- 46 S. Gronthos, A. C. Zannettino, S. E. Graves, S. Ohta, S. J. Hay and P. J. Simmons, *J Bone Miner Res*, 1999, **14**, 47-56.
- 47 G. J. Atkins, P. Kostakis, B. Pan, A. Farrugia, S. Gronthos, A. Evdokiou, K. Harrison, D. M. Findlay and A. C. Zannettino, *J Bone Miner Res*, 2003, **18**, 1088-1098.
- 48 S. L. Dallas, M. Prideaux and L. F. Bonewald, *Endocr Rev*, 2013, **34**, 658-690.
- 49 G. Atkins and D. Findlay, *Osteoporosis international*, 2012, **23**, 2067-2079.
- 50 J. Cubo, M. Hui, F. Clarac and A. Quilhac, *J Morphol*, 2017, **278**, 621-628.
- 51 H. Chen, T. Senda and K. Y. Kubo, *Med Mol Morphol*, 2015, **48**, 61-68.
- 52 H. W. Kim, H. E. Kim and J. C. Knowles, *Biomaterials*, 2004, **25**, 3351-3358.
- 53 T. A. Franz-Odenaal, B. K. Hall and P. E. Witten, *Dev Dyn*, 2006, **235**, 176-190.
- 54 G. J. Atkins, P. S. Rowe, H. P. Lim, K. J. Welldon, R. Ormsby, A. R. Wijenayaka, L. Zelenchuk, A. Evdokiou and D. M. Findlay, *J Bone Mineral Research*, 2011, **26**, 1425-1436.
- 55 Y. L. Chang, C. M. Stanford and J. C. Keller, *J Biomed Mater Res*, 2000, **52**, 270-278.
- 56 K. J. Welldon, D. M. Findlay, A. Evdokiou, R. T. Ormsby and G. J. Atkins, *Mol cellular endocrinol*, 2013, **376**, 85-92.



1234x1068mm (72 x 72 DPI)